

Nitrogen-induced ELM suppression and confinement improvement in the EAST tokamak with a full metal wall

Jingyan Hu¹, Peng Shi^{2,*}, Chu Zhou³, Jinyue Liu², Gongshun Li², Kangning Geng², Yiren Zhu⁴, Kedong Li², Hailin Zhao², Xiang Jian², and Ge Zhuang³

¹School of the Gifted Young, University of Science and Technology of China, Hefei 230026, China

²Institute of Plasma Physics, Chinese Academy of Sciences, Hefei 230031, China

³School of Nuclear Science and Technology, University of Science and Technology of China, Hefei 230026, China

⁴Southwestern Institute of Physics, PO Box 432, Chengdu 610041, China

May 28, 2026

Abstract

This paper reports the achievement of an ELM-free H-mode regime with confinement improvement enabled by nitrogen (N_2) seeding on the Experimental Advanced Superconducting Tokamak (EAST) with a full metal wall. Following N_2 injection, large Edge-Localized Mode (ELM) bursts are completely suppressed, while global energy confinement is significantly enhanced, with the $H_{98(y,2)}$ factor increasing from approximately 0.9 to 1.2. A distinct edge coherent mode (ECM), localized at the pedestal foot ($\psi_N \sim 0.99$), is identified using O-mode Poloidal Correlation Reflectometry and AXUV diagnostics. This mode operates within a frequency range of 20–50 kHz with a poloidal wavenumber of $k_\theta \approx 0.54 \text{ cm}^{-1}$. Linear gyrokinetic simulations performed with the CGYRO code reveal a dominant instability that quantitatively matches the experimental measurements. Detailed scans of parameters identify this mode as a Dissipative Trapped Electron Mode (DTEM). The energy and particle transport driven by this pedestal-foot DTEM effectively regulates the edge gradients, preventing the pedestal from crossing the Peeling-Ballooning stability boundary and sustaining a stationary ELM-free state. These findings provide a physical basis for an integrated scenario to maintain high confinement and protect plasma-facing components in future steady-state fusion reactors.

1 Introduction

The High-Confinement Mode (H-mode), characterized by elevated core density and temperature [1], represents a primary operational scenario for magnetic confinement fusion devices aiming to achieve the requisite fusion triple product $nT\tau_E$ and ignition condition [2, 3, 4].

*Email: pshi@ipp.ac.cn

In H-mode, an edge transport barrier known as the pedestal forms [1, 5], which significantly reduces turbulent transport and sustains the high core confinement [6].

However, the steep pressure gradients and associated bootstrap currents in the pedestal can trigger Peeling-Ballooning (PB) instabilities [3, 6].

As the pedestal evolves, pressure and current density profiles eventually breach the P-B stability boundary and trigger Edge-Localized Modes (ELMs) [5].

ELMs expel bursts of particles and energy into the Scrape-Off Layer (SOL) and induce transient heat fluxes onto plasma-facing components (PFCs) [7]. In reactor-scale plasmas, these transients can impose damaging heat loads on divertor targets and other PFCs, posing a significant threat to the longevity of steady-state reactors [8, 9]. The problem is expected to become more restrictive in future burning plasma devices (e.g., ITER) [10], where smaller normalized ion gyro-radii (ρ_i) and collisionality can reduce diamagnetic stabilization of medium n P-B modes [5, 7]. Therefore, developing integrated control scenarios that suppress ELMs while maintaining high confinement remains a primary goal for steady-state fusion operation.

Currently, several active ELM-control methods have been developed, including pellet pacing [11], Resonant Magnetic Perturbations (RMP) [12], and impurity powder injection (e.g., Lithium, Boron) [13]. While effective in certain regimes, these methods face challenges regarding engineering complexity, operational windows (e.g., q_{95} restrictions for RMP), and compatibility with reactor-grade fueling or wall-conditioning requirements [14, 7].

Impurity gas seeding offers a flexible alternative. In future metallic-wall reactors like ITER, low- Z species such as Nitrogen (N_2), Neon (Ne), and Argon (Ar) are generally categorized as low- Z impurities, distinct from high- Z intrinsic metallic impurities. Seeding these low- Z impurities can increase edge radiation and help manage steady-state power exhaust. In current tokamaks, low- Z impurity injection has been shown to successfully enable access to ELM-mitigated or ELM-suppressed regimes, and sometimes can achieve divertor detachment simultaneously [15, 16, 17, 18, 19]. However, its impact on pedestal stability and plasma confinement is not universal [15, 18, 17]. Optimized seeding can access small- or no-ELM regimes and even improve confinement [15], whereas excessive radiation, fuel dilution, or unfavorable edge profile changes can degrade performance [16, 18, 17].

This non-universality points to an unresolved physics question: how impurity seeding modifies the pedestal transport channels that determine whether the plasma relaxes gently or enters large ELM cycles. Previous EAST studies have shown that specific turbulence, such as edge coherent modes [20] and high-frequency broadband turbulence [21], can provide continuous transport and regulate ELM activity in long-pulse H-mode plasmas.

Here we report on a nitrogen-induced ELM-free H-mode regime on EAST with a full metal wall. After Nitrogen injection, large ELMs are suppressed while the global confinement improves, with $H_{98(y,2)}$ increasing from about 0.9 to 1.2. Using O-mode poloidal correlation reflectometry (PCR), absolute extreme-ultraviolet (AXUV) arrays and magnetic diagnostics, we identify a predominantly electrostatic edge coherent mode. Distinct from the typical Edge Harmonic Oscillations (EHO) [22] or Edge Coherent Modes (ECM) [23] often observed in the steep-gradient region, the ECM found here is localized at the pedestal foot. This mode operates within a frequency range of 20–50 kHz, with a poloidal wavelength of approximately 11.7 cm.

Linear gyrokinetic simulations with CGYRO show that the measured wavenumber, propagation direction and eigenfunction parity are consistent with a dissipative trapped electron mode (DTEM). Parameter scans further show that this mode is driven by the electron temperature gradients and is destabilized by the enhanced collisionality associated with nitrogen seeding. However, the ELM-free phase is accompanied by a stronger temperature pedestal and improved global confinement. ELITE analysis also indicates a higher linear peeling-ballooning growth rate after ELM suppression. These observations rule out a simple pressure-gradient-clamping explanation. We therefore propose that the nitrogen-induced ECM suppresses ELMs through nonlinear interaction with peeling-ballooning dynamics, consistent with coherent-mode-mediated ELM mitigation mechanisms reported in recent EAST simulations [24] and multiscale tokamak-edge studies [25].

2 Experimental Setup

The experiments were conducted on the Experimental Advanced Superconducting Tokamak (EAST) [26], which was operated in a single-null divertor configuration. This device is equipped with ITER-like water-cooled tungsten (W) monoblocks as plasma-facing components (PFCs) for handling high heat fluxes. To access the H-mode and sustain the plasma performance in this discharge, auxiliary heating was provided by a combination of Electron Cyclotron Resonance Heating (ECRH) and Neutral Beam Injection (NBI).

To comprehensively evaluate the plasma response to nitrogen seeding, a suite of high-resolution diagnostic systems was employed, as illustrated in Fig. 1. Electron density (n_e) profiles were provided by the Density Profile Reflectometry (DPR) system [27]. Electron temperature (T_e) profiles were reconstructed from Thomson scattering measurements [28] and the Electron Cyclotron Emission (ECE) data [29].

Pedestal fluctuations and coherent modes were diagnosed with complementary microwave systems covering different radial locations. Doppler Backscattering (DBS) system, operating in X-mode over the W-band (75–110 GHz) [30], probed the pedestal top and steep-gradient region. Poloidal Correlation Reflectometry (PCR) system, operated in O-mode over the K-Ka band (20.4–40 GHz) [31] and the U-band (42.4–57.2 GHz) [32, 33], monitored the middle-to-lower pedestal with partial overlap with the DBS measurement region.

The radiative cooling and impurity penetration were assessed using absolute extreme ultraviolet (AXUV) photodiode arrays [34] and extreme ultraviolet (EUV) spectroscopy [35]. The AXUV system comprises four horizontal arrays with a total of 64 channels, providing extensive coverage of the plasma cross-section. Furthermore, the N_{VII} line emission intensity measured by EUV spectroscopy was used as a proxy for nitrogen penetration and ionization state in the bulk plasma. Additionally, ELM activity and magnetic fluctuations were monitored using D_α emission arrays and magnetic Mirnov coils.

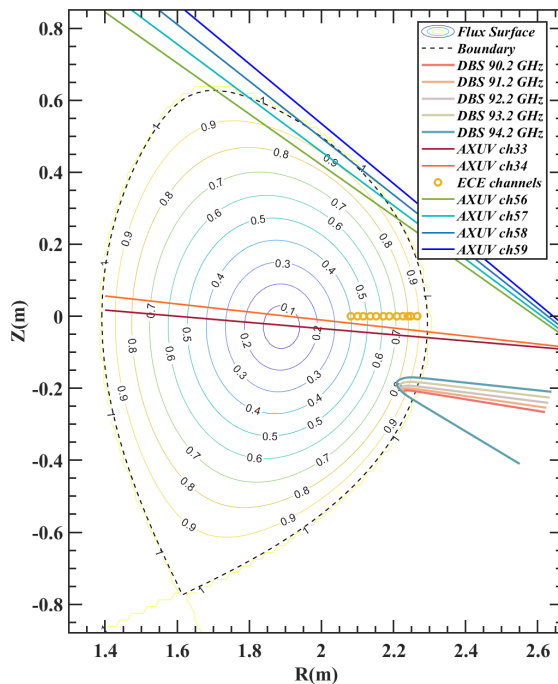


Figure 1: Overview of the experimental diagnostics and equilibrium configuration. The reflectometry for density measurements is located 3 cm above the midplane. ECE channels are positioned near the low-field side (LFS). The flux surfaces represent the reconstructed equilibrium for discharge #153901.

3 Phenomenology of ELM suppression and data analysis

3.1 Macroscopic evolution and pedestal profiles

The temporal evolution of key plasma parameters for the representative Nitrogen-seeded discharge (#153901) is displayed in Fig. 2. The target H-mode plasma was operated with a plasma current of $I_p \approx 450$ kA, an edge safety factor of $q_{95} \approx 5.3$, a normalized energy confinement factor $H_{98(y,2)} \approx 1.0$ and a line-averaged electron density of $n_e \approx 5.2 \times 10^{19} \text{ m}^{-3}$ (corresponds to a Greenwald density fraction of $f_{GW} \approx 0.74$). Prior to impurity injection, the discharge exhibited ELMy H-mode characteristics.

To achieve and sustain the H-mode regime at high plasma beta, a total of 2.7 MW of auxiliary heating was applied, consisting of 1.35 MW of NBI and 1.35 MW of ECRH. The NBI system was active from $t = 4.0$ s to 10.0 s, while the ECRH system provided continuous heating from $t = 0.0$ s to 10.9 s, fully covering the impurity injection window.

Nitrogen seeding was applied using a localized impurity gas injection system. A gas mixture of 50% N_2 and 50% D_2 was injected from the low-field side midplane during the commanded puff interval of $t = 5.0$ -6.0 s. The actual impurity arrival in the plasma was identified from the boundary AXUV channel 59 and the EUV nitrogen radiation signal. The increase of boundary AXUV and nitrogen radiation indicate that N_2 entered the plasma at approximately 5.25 s, corresponding to a delay of about 0.25 s from the gas inlet to the plasma. Therefore, the

shaded region in Fig. 2 denotes the time interval after impurity penetration into the plasma.

After nitrogen entered the plasma, the line-averaged density remained nearly unchanged under feedback control, whereas the core and edge radiation increased. ECE measurements show that both core and edge temperatures rose during the seeding phase. Consistently, the plasma stored energy W_{MHD} increased from approximately 160 kJ to 200 kJ, and $H_{98(y2)}$ increased from 0.9 to 1.2. At the same time, the D_α spikes and Mirnov bursts were progressively weakened and then fully suppressed at approximately 6.1 s; this ELM-free phase persisted until about 6.95 s.

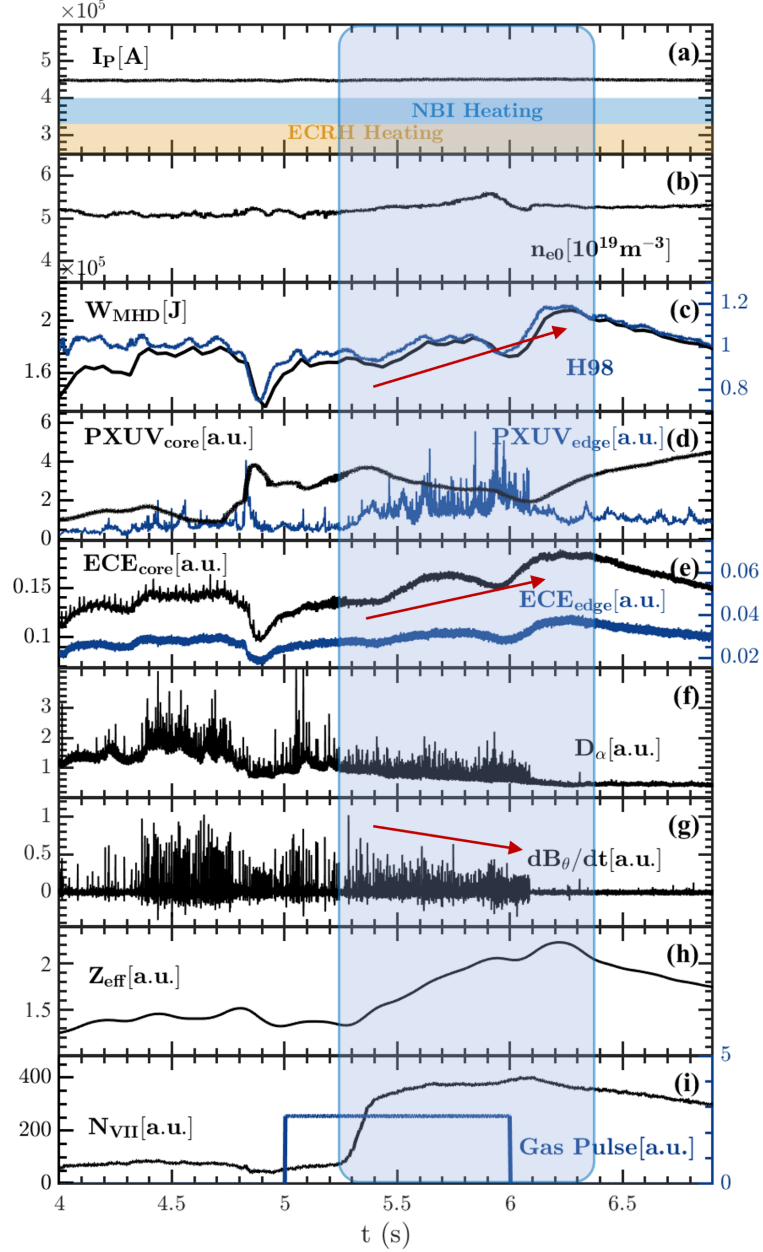


Figure 2: Time evolution of main parameters for EAST discharge #153901: (a) Plasma current I_p and auxiliary heating (NBI and ECRH), (b) line-averaged electron density \bar{n}_e , (c) plasma stored energy W_{MHD} and confinement factor $H_{98(y,2)}$, (d) core and edge PXUV radiation, (e) core and edge ECE temperature signals, (f) divertor D_α emission, (g) magnetic Mirnov coil signal, (h) effective nuclear charge Z_{eff} , (i) N_{VII} emission and N_2 gas puffing pulse.

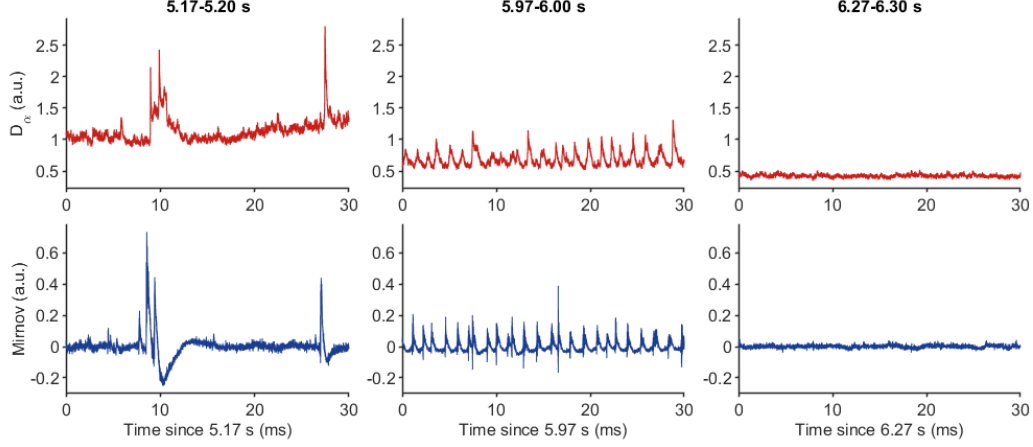


Figure 3: Expanded D_α and Mirnov signals in three representative time windows. The ELM activity changes from large-amplitude, low-frequency Type-I ELMs before impurity penetration (5.17-5.20 s) to small-amplitude, high-frequency Type-III ELMs around 6.0 s (5.97-6.00 s), and then to an ELM-free phase at 6.27-6.30 s.

Fig. 3 further resolves the change in ELM behavior during the nitrogen-seeding sequence. Before impurity penetration, at around 5.2 s, the D_α and Mirnov signals show large, isolated bursts with an ELM repetition frequency of about 50 Hz, identifying them as Type-I ELMs; this classification is consistent with the ELITE linear stability result for the pre-seeding pedestal. At around 6.0 s, the burst amplitude is strongly reduced while the repetition frequency increases to about 600 Hz, indicating a transition to Type-III ELMs. By 6.27-6.30 s, both D_α spikes and Mirnov bursts are strongly suppressed, marking the ELM-free stage.

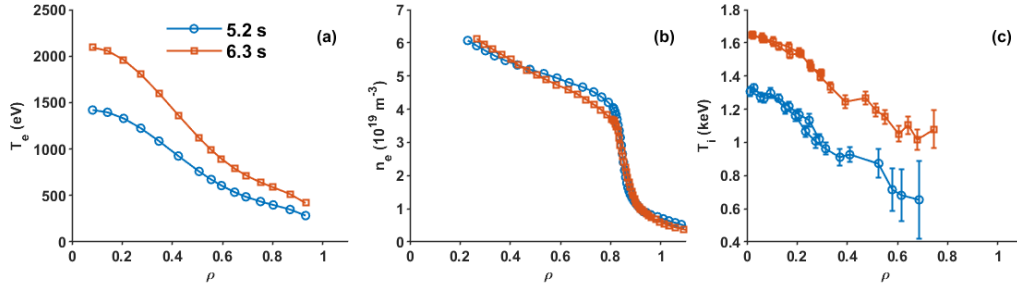


Figure 4: Comparison of electron temperature, electron density and ion temperature profiles for EAST discharge #153901 at 5.2 s (blue) and 6.3 s (red). The profiles show a pronounced increase in the electron and ion temperatures, together with a modest relaxation of the pedestal density gradient, after nitrogen entered the plasma.

The profile comparison in Fig. 4 shows that ELM suppression is accompanied by improved confinement rather than pedestal degradation. Both electron and ion temperatures increase after nitrogen entered the plasma, whereas the electron density pedestal is slightly relaxed. This channel-dependent profile evolution is consistent with the increase in stored energy and $H_{98(y2)}$ shown in Fig. 2. It also argues against a simple pressure-gradient-clamping interpretation of ELM suppression. The following sections therefore focus on the edge coherent mode that appears during this high-confinement ELM-free phase and on its role in the nonlinear ELM-suppression mechanism.

3.2 Spectral features and radial localization

The Doppler backscattering (DBS) system operated in X-mode at 90.2-94.2 GHz and sampled the pedestal top and steep-gradient region. Before impurity penetration, the DBS spectrogram in Fig. 5 shows a pre-existing edge coherent mode (ECM) at 20-90 kHz. This mode is localized near the steep-gradient pedestal region ($\psi_N \approx 0.95$) and is consistent with the electrostatic ECM commonly observed in EAST H-mode plasmas, where it is identified as Trapped Electron Mode (TEM) [23, 36].

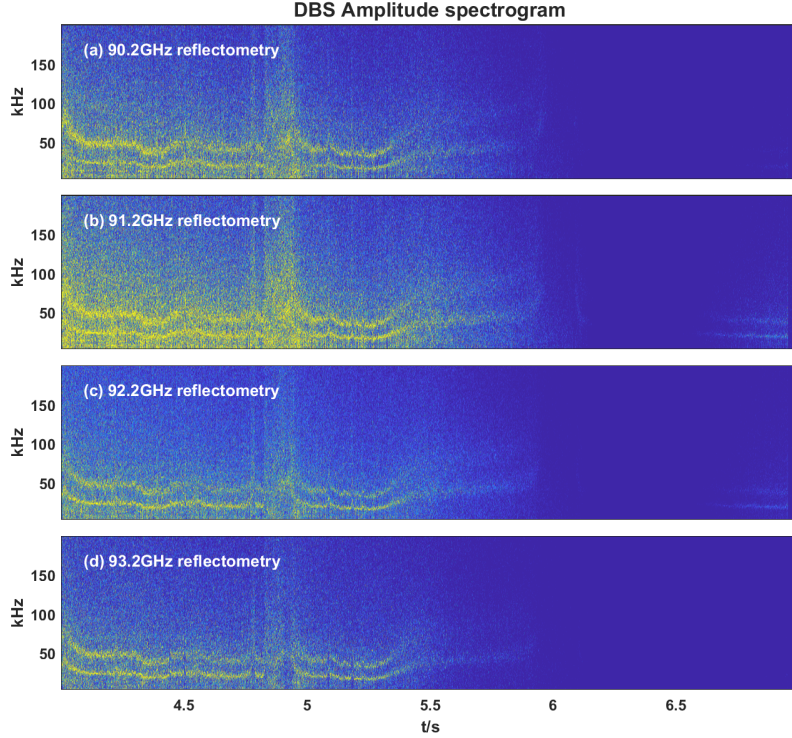


Figure 5: Doppler Backscattering

After nitrogen entered the plasma, broadband pedestal turbulence in the DBS amplitude spectrogram was almost completely suppressed, and the pre-existing ECM disappeared. At the same time, the PCR signals in Fig. 6 show the emergence of a new coherent fluctuation at the pedestal foot in the 24.8 GHz channel. The mode frequency chirps downward from approximately 40 kHz to 20 kHz, and its onset coincides with complete ELM suppression.

O-mode reflectometry provides an initial radial constraint on this new mode. The coherent fluctuation is clearly detected by the 24.8 GHz channel but is absent from the 20.4 GHz channel. Because each channel is most sensitive to density fluctuations near its cutoff layer, this contrast places the mode between the corresponding cutoff layers, namely near the pedestal foot.

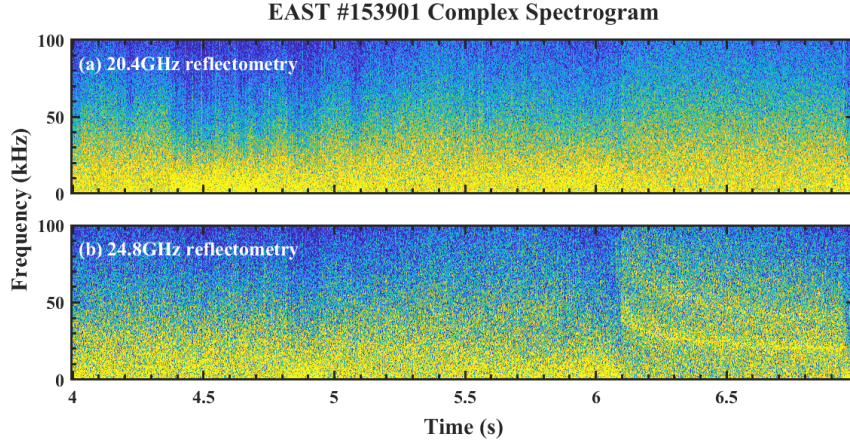


Figure 6: K/Ka band of the Poloidal Correlation Reflectometry, the detected complex signal is expressed as $I + iQ$.

Further inward, the U-band reflectometry data in Fig. 7 further separate the pre- and post-suppression modes. These inner channels detect both the original ECM before ELM suppression and the new coherent mode after suppression. The post-suppression mode has a larger fluctuation amplitude than the original ECM, but it is observed at a more outward cutoff region. Since the original ECM is detected by the inner probing channels but not by the 24.8 GHz channel, it is localized between the 42.4 GHz and 24.8 GHz cutoff layers, closer to the steep-gradient pedestal region than the new pedestal-foot mode.

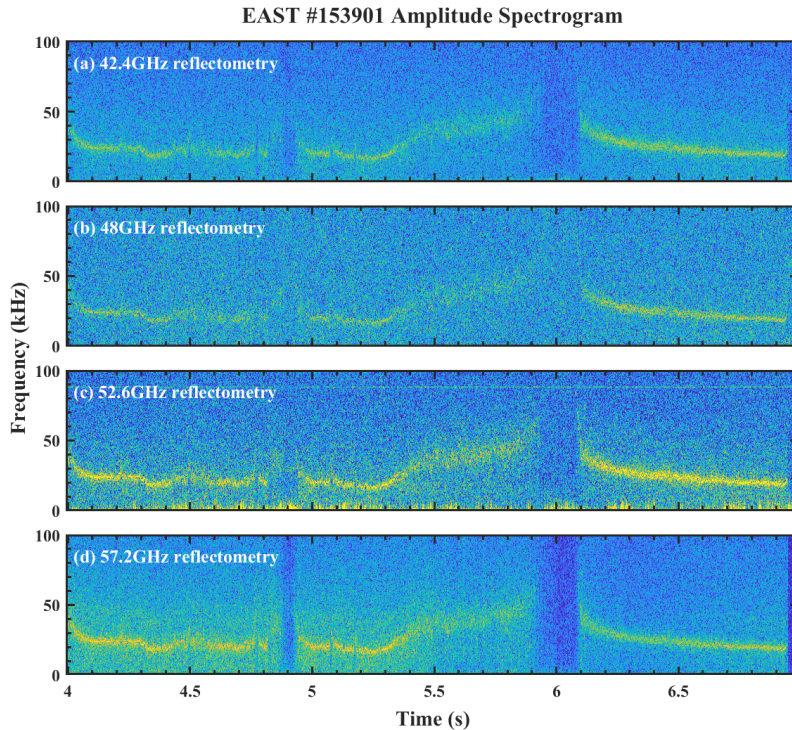


Figure 7: U band of the Poloidal Correlation Reflectometry

To convert these frequency constraints into radial locations, the reflectometry probing frequencies are mapped onto the measured electron-density profiles. As shown in Fig. 8 for $t=5.2$ s

and $t=6.3$ s, the cutoff layers for the higher-frequency channels (33-52.6 GHz) lie in the steep-gradient region, whereas the 24.8 GHz cutoff is located near the pedestal foot ($R \approx 2.29$ m, $\psi_N \approx 0.98 - 0.99$). The 20.4 GHz cutoff is farther outward in the scrape-off layer and shows no coherent fluctuation. Taken together, the DBS, K/Ka-band and U-band reflectometry measurements localize the new 20-50 kHz mode to a narrow pedestal-foot layer.

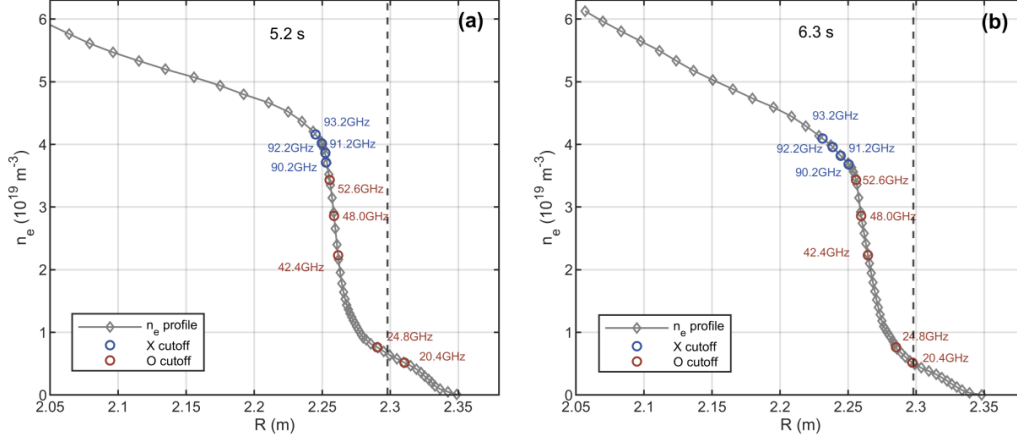


Figure 8: Density profile measured by reflectometry, with the locations of the cutoff corresponding to different frequencies.

The AXUV bolometer arrays provide an independent check of this localization. Because the AXUV signals are line-integrated along the viewing chords, the radial position of a localized mode can be constrained by comparing adjacent channels. As shown in Fig. 9, the coherent fluctuation is visible in channels 56 and 57 but is absent from the outer channels 58 and 59. The mode is therefore constrained to lie between the tangent radii of AXUV channels 57 and 58, consistent with the pedestal-foot location inferred from reflectometry.

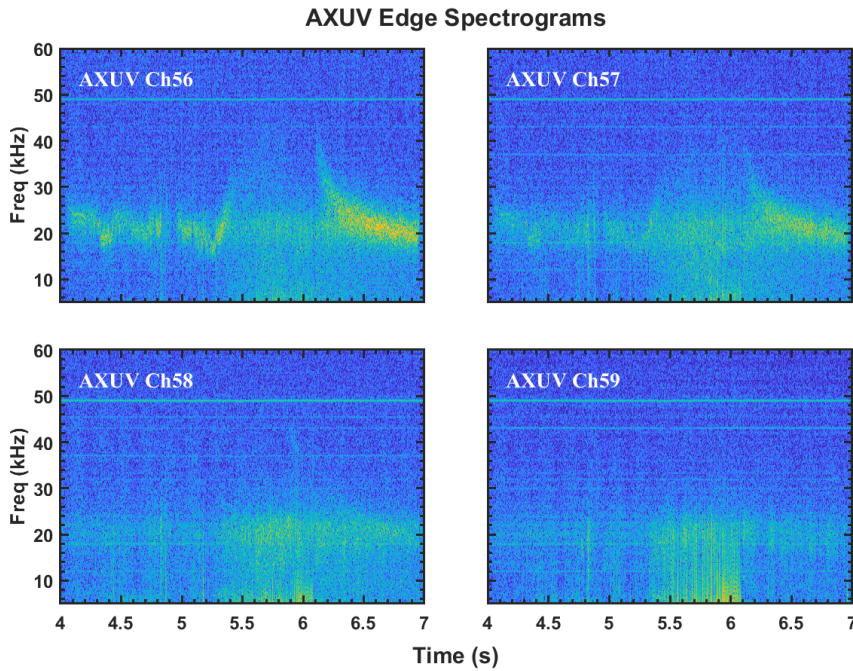


Figure 9: Spectrograms of edge AXUV

This cross-diagnostic consistency is important. Reflectometry excludes the steep-gradient region and the scrape-off layer as the primary location of the new mode, while the AXUV channel pattern independently confines it to the same edge layer. The nitrogen-induced coherent mode is therefore displaced outward from the pre-seeding ECM and resides in the pedestal foot.

The AXUV spectrograms in Fig. 9 also show that the post-seeding coherent fluctuation has a larger radiative fluctuation amplitude than the pre-seeding ECM.

An analysis of the high-frequency Mirnov coil signals in Fig. 10 reveals no corresponding magnetic fluctuation in the 20-50 kHz range. This magnetic-null result indicates that the observed coherent mode is predominantly electrostatic.

We therefore conclude that nitrogen seeding does not simply strengthen the pre-existing steep-gradient ECM. Instead, it replaces it with a new, radially outward and predominantly electrostatic coherent mode at the pedestal foot ($\psi_N \approx 0.98 - 0.99$). This localization and magnetic-null result distinguish the observed mode from typical electromagnetic EHO/ECM activity located closer to the steep-gradient pedestal [22].

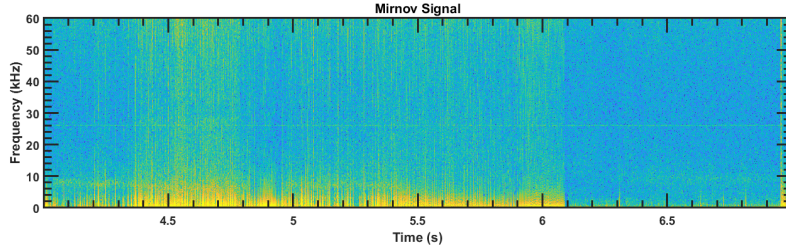


Figure 10: Mirnov Signal

3.3 Mode number analysis and dispersion relation

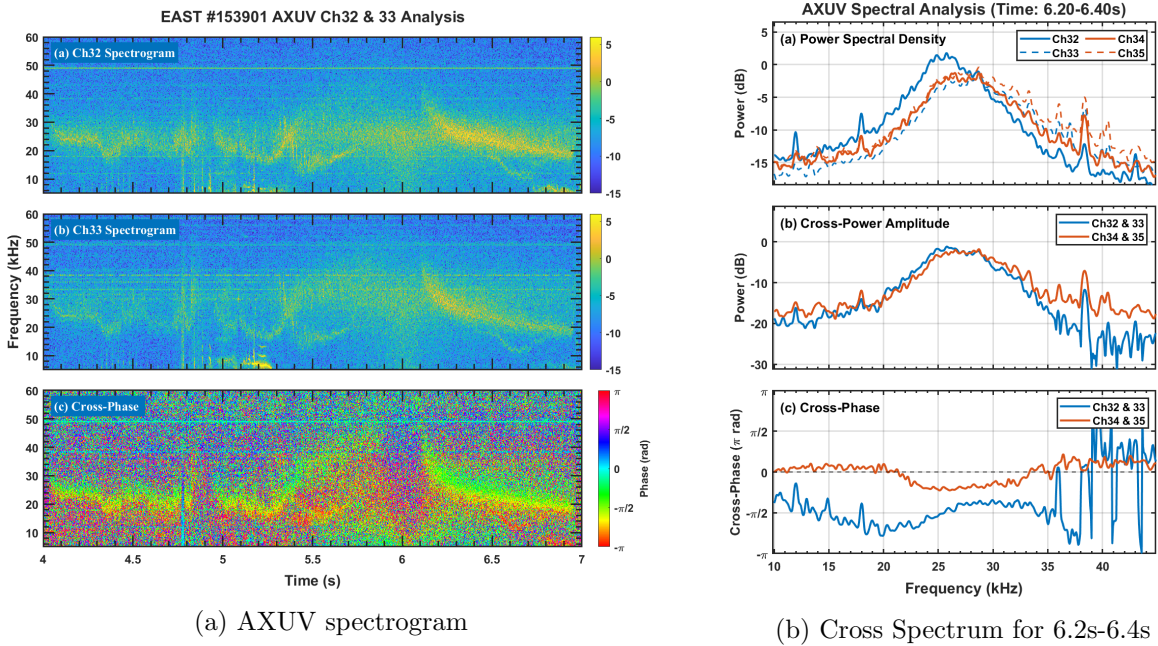


Figure 11: AXUV Correlation Analysis

After the radial localization was established, the poloidal wavenumber k_θ and the mode numbers (m, n) were estimated from the cross-phase between adjacent AXUV midplane channels, as shown in Fig. 11a. The calculation uses local quantities at the mode position: the safety factor $q \approx 9.3$ from magnetic equilibrium reconstruction, the electron temperature $T_e \approx 180$ eV from the measured profiles (Fig. 4), and the local magnetic field $B \approx 5.3$ T. The relevant separation Δl_{pol} is the distance between the two intersection points where the localized mode crosses the two AXUV viewing chords on the same flux surface, rather than a purely geometrical chord projection. The poloidal wavenumber is then derived as

$$k_\theta = \frac{\Delta\Phi}{\Delta l_{\text{pol}}}, \quad (1)$$

where $\Delta\Phi$ is the measured phase shift at the center frequency of the mode. From the cross-power spectrum in Fig. 11b(c), the phase shift at the dominant frequency is obtained as $\Delta\Phi \approx 0.3\pi$; the negative sign of the raw phase shift simply indicates the propagation direction of the mode.

Using these parameters, the poloidal wavenumber is $k_\theta \approx 0.538$ cm⁻¹. With the local magnetic pitch angle, this gives a toroidal mode number $n \approx 13$. Combining this with the local safety factor $q = m/n \approx 9.3$ gives a poloidal mode number $m \approx 123$. The wavenumber is then normalized to the ion sound Larmor radius, $\rho_s = \sqrt{m_i T_e}/eB$, which is approximately 0.0366 cm for the local plasma parameters. The resulting normalized wavenumber is $k_\theta \rho_s \approx 0.0197$.

These measurements establish the key experimental constraints on the mode: it is localized at the pedestal foot, predominantly electrostatic, and characterized by a low normalized wavenumber. However, these observables alone do not uniquely identify the underlying micro-instability, such as a trapped electron mode or an ion temperature gradient mode. The physical nature of the mode and the role of the local driving gradients are therefore examined using linear gyrokinetic simulations in the following section.

4 Characterization of the pedestal foot mode with CGYRO

4.1 Plasma profiles and simulation setup

To identify the micro-instability associated with the coherent mode at the pedestal foot, linear gyrokinetic simulations were performed with CGYRO. The calculations used experimentally constrained local profiles from EAST discharge #153901 during the stationary ELM-free phase at $t = 6.3$ s. The simulation surface was chosen at $\psi_N = 0.99$, where the 20–50 kHz coherent fluctuation is localized by the reflectometry and AXUV measurements.

At this radial location, the local plasma parameters are characterized by steep electron temperature and density gradients, with the normalized electron temperature gradient $a/L_{T_e} = 151.87$ and the normalized electron density gradient $a/L_{n_e} = 44.13$, and by a local safety factor $q = 9.29$. Because the surface is close to the separatrix, the magnetic shear is very high ($\hat{s} \approx 65$). Nitrogen seeding also increases the effective charge to $Z_{eff} \approx 2.03$, giving a relatively high normalized electron collisionality $\nu_e \approx 1.13$. These local conditions provide the input needed to test whether the measured ECM is compatible with a collisional trapped-electron

instability.

The kinetic profiles used in the simulations were constrained by multiple diagnostics. The electron density and temperature profiles were obtained from reflectometry and Thomson scattering, with consistency checked against ECE measurements. The ion temperature profile was provided by X-ray crystal spectroscopy (XCS), and the magnetic equilibrium was reconstructed with EFIT and cross-validated by ONETWO integrated modeling. Both electrostatic and electromagnetic perturbations were retained in the calculation, and a high poloidal grid resolution along the extended ballooning angle was used to resolve the mode structure in this high-collisionality, high-shear edge region.

4.2 Linear Growth Rate and Eigenfunction Analysis

The linear stability characteristics of the observed mode were then examined with CGYRO. Fig. 12 shows the spectra of the normalized linear growth rate γ and real frequency ω as functions of the normalized binormal wavenumber $k_y \rho_s$. The real frequency is negative over the relevant wavenumber range, indicating propagation in the electron diamagnetic drift direction. This propagation direction is inconsistent with an ion temperature gradient (ITG) mode [37, 38].

The dominant instability peaks at a low wavenumber, $k_y \rho_s \approx 0.022$, corresponding to a physical wavenumber $k_y \approx 0.47 \text{ cm}^{-1}$. This value agrees well with the experimentally inferred poloidal wavenumber $k_\theta \approx 0.54 \text{ cm}^{-1}$ from AXUV cross-phase analysis. The low- k_y scale is also far below the range expected for electron temperature gradient (ETG) modes, which typically occur at $k_y \rho_s$ of order unity or higher [39, 37, 40].

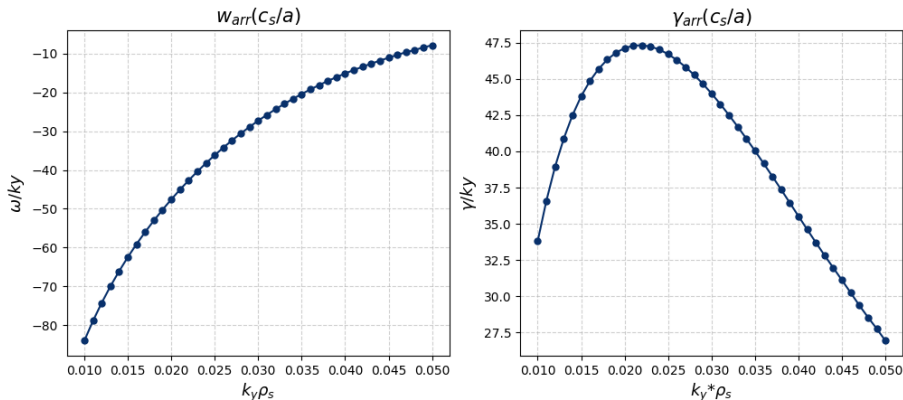


Figure 12: Real frequency ω and normalized linear growth rate γ spectra as functions of the normalized wavenumber $k_y \rho_s$ at $\psi_N = 0.99$ for $t = 6.3 \text{ s}$.

The eigenfunctions of the electrostatic potential ϕ and the parallel magnetic vector potential A_{\parallel} provide an additional constraint on the mode identification ((Fig. 13) [39]). The potential ϕ has a localized, even-parity structure centered near the outboard midplane ($\theta = 0$), while A_{\parallel} is much weaker and shows a mixed-parity structure. Together with the electron-directed propagation and the low normalized wavenumber, these eigenfunction properties identify the instability as a trapped electron mode (TEM). Furthermore, the dominantly electrostatic character of the

calculated mode is also consistent with the absence of a corresponding 20–50 kHz Mirnov signal in the experiment.

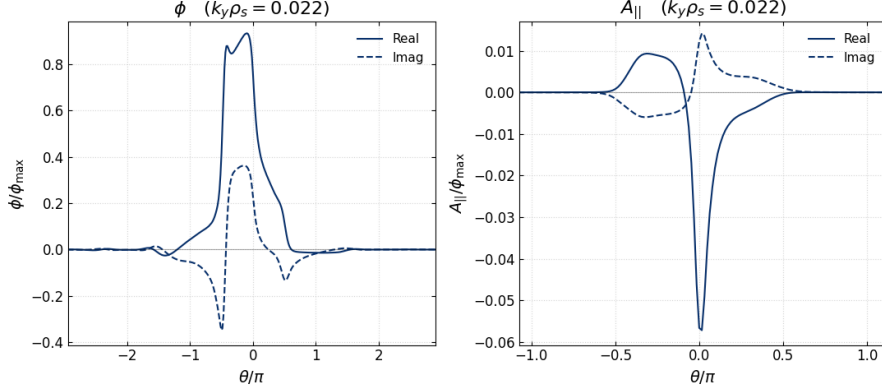


Figure 13: Eigen Functions of $k=0.022$

4.3 Parametric Dependence and Identification of DTEM

To further classify the instability, parametric scans were performed in the normalized density gradient a/L_{n_e} , electron temperature gradient a/L_{T_e} and electron collisionality ν_e . As shown in Fig. 14a and 14b, the linear growth rate significantly increases with electron temperature gradient, but is weakly related to density gradient. This indicates that the mode is a TEM driven by electron temperature gradient [41].

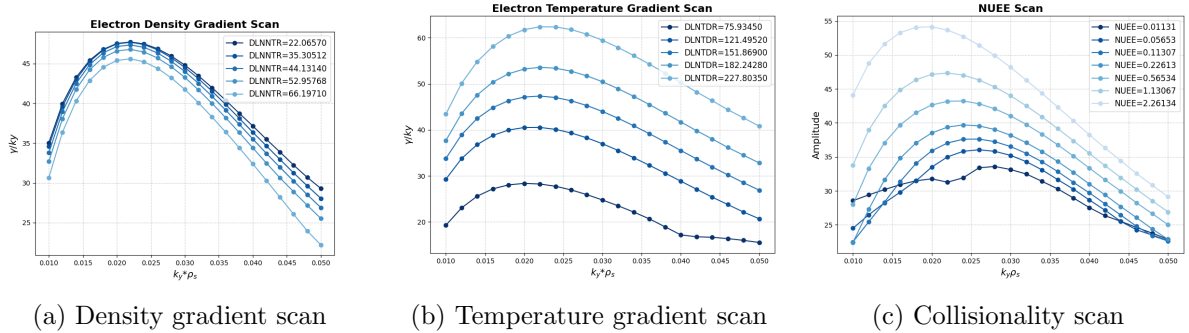


Figure 14: Parametric dependencies of the normalized linear growth rate at $k_y\rho_s = 0.022$ on (a) normalized density gradient a/L_{n_e} , (b) normalized temperature gradient a/L_{T_e} , and (c) normalized electron collisionality ν_e .

The collisionality scan in Fig. 14c provides the key distinction between a collisionless TEM and a dissipative TEM. Increasing ν_e further destabilizes the mode, whereas collisions would normally reduce the drive of a collisionless TEM by detrapping electrons. This positive collisionality dependence, together with the electrostatic eigenfunction and the absence of a magnetic Mirnov counterpart, supports identification of the observed pedestal-foot ECM as a dissipative trapped electron mode (DTEM), rather than a micro-tearing mode [41, 42].

Overall, the CGYRO results reproduce the main experimental constraints on the ECM: the low normalized wavenumber, electron-diamagnetic propagation, predominantly electrostatic character and sensitivity to the nitrogen-modified edge collisionality and gradients. The simu-

lations therefore identify the 20–50 kHz pedestal-foot ECM as a DTEM-like instability excited under the local edge conditions after nitrogen seeding.

5 Discussion and Conclusion

The combined measurements show that nitrogen seeding substantially changes the edge fluctuation state while maintaining improved confinement. After nitrogen enters the plasma, the pre-existing ECM in the steep-gradient region disappears and a new 20–50 kHz ECM appears at the pedestal foot. At the same time, the ELM activity evolves from large Type-I events to small, high-frequency Type-III ELMs and finally to an ELM-free state, while the temperature pedestal, stored energy and $H_{98(y,2)}$ increase.

A critical constraint comes from the ELITE linear stability analysis. In the ELM-free phase, the linear growth rate of the P-B instability is higher than that before ELM suppression. Therefore, the disappearance of large ELM crashes cannot be explained by a simple reduction of the pedestal pressure gradient or by moving the pedestal farther away from the P-B stability boundary. Instead, the observations indicate that the nitrogen-induced ECM modifies the nonlinear evolution of the P-B instability.

This interpretation is consistent with coherent-mode-mediated ELM mitigation mechanisms reported in recent EAST simulations and multiscale edge studies [36, 25], where an edge coherent mode can alter the growth, phase coherence, saturation or energy-transfer pathway of P-B modes through nonlinear interaction.

Reflectometry and AXUV measurements identify the new 20–50 kHz ECM localized at the pedestal foot ($\psi_N \approx 0.98 - 0.99$), with no clear magnetic counterpart in Mirnov coils and with $k_\theta \approx 0.5\text{--}0.6 \text{ cm}^{-1}$. Linear gyrokinetic simulations with CGYRO reproduce the measured electron-direction propagation and low normalized wavenumber, $k_y \rho_s = 0.022$ (corresponding to $k_y \approx 0.47 \text{ cm}^{-1}$), and parameter scans identify the mode as a dissipative trapped electron mode driven by the nitrogen-modified edge conditions.

Together with ELITE results showing an increased P-B linear growth rate in the ELM-free phase, these observations indicate that ELM suppression is not caused by simple weakening of the pedestal drive. Instead, the results support a coherent-mode-mediated nonlinear interaction between the pedestal-foot ECM and P-B dynamics. Future nonlinear BOUT++ simulations based on the measured pedestal profiles will therefore be needed to determine how this ECM suppresses large ELM crashes while preserving the improved-confinement pedestal.

Acknowledgments

This work is supported by the National MCF Energy R&D Program under Grant No. 2024YFE-03060004. We thank the EAST team (<https://cstr.cn/31130.02.EAST>), for providing technical support and assistance in data collection and analysis. We also express our sincere gratitude to Li Yanlong for the valuable discussions regarding the BOUT++ simulations.

References

- [1] Fritz Wagner et al. “Regime of improved confinement and high beta in neutral-beam-heated divertor discharges of the ASDEX tokamak”. In: *Physical Review Letters* 49.19 (1982), p. 1408.
- [2] John D Lawson. “Some criteria for a power producing thermonuclear reactor”. In: *Proceedings of the physical society. Section B* 70.1 (1957), pp. 6–10.
- [3] JW Connor et al. “Magnetohydrodynamic stability of tokamak edge plasmas”. In: *Physics of plasmas* 5.7 (1998), pp. 2687–2700.
- [4] JR McNally Jr. “Nuclear data in science and technology”. In: *Proc. Int. Conf.(Paris, 1973)*. Vol. 2. 1973, p. 41.
- [5] PB Snyder et al. “ELMs and constraints on the H-mode pedestal: peeling–ballooning stability calculation and comparison with experiment”. In: *Nuclear fusion* 44.2 (2004), pp. 320–328.
- [6] Hajime Urano. “Pedestal structure in H-mode plasmas”. In: *Nuclear Fusion* 54.11 (2014), p. 116001.
- [7] GTA Huijsmans et al. “Modelling of edge localised modes and edge localised mode control”. In: *Physics of Plasmas* 22.2 (2015).
- [8] AW Leonard et al. “The impact of ELMs on the ITER divertor”. In: *Journal of nuclear materials* 266 (1999), pp. 109–117.
- [9] A Herrmann et al. “Stationary and transient divertor heat flux profiles and extrapolation to ITER”. In: *Journal of nuclear materials* 313 (2003), pp. 759–767.
- [10] PB Snyder et al. “Pedestal stability comparison and ITER pedestal prediction”. In: *Nuclear Fusion* 49.8 (2009), p. 085035.
- [11] GW Pacher et al. “ELM pacing and the ITER operating window: mutual constraints”. In: *Nuclear Fusion* 51.8 (2011), p. 083004.
- [12] Richard Fitzpatrick. “Modeling q95 windows for the suppression of edge localized modes by resonant magnetic perturbations in the DIII-D tokamak”. In: *Physics of Plasmas* 27.10 (2020).
- [13] Z Sun et al. “Suppression of edge localized modes with real-time boron injection using the tungsten divertor in EAST”. In: *Nuclear Fusion* 61.1 (2021), p. 014002.
- [14] PT Lang et al. “ELM control strategies and tools: status and potential for ITER”. In: *Nuclear Fusion* 53.4 (2013), p. 043004.
- [15] K Li et al. “Compatibility of large ELM control and stable partial detachment with neon/argon seeding in EAST”. In: *Nuclear Fusion* 63.2 (2023), p. 026025.
- [16] J Rapp et al. “ELM mitigation by nitrogen seeding in the JET gas box divertor”. In: *Plasma physics and controlled fusion* 44.6 (2002), pp. 639–652.

- [17] L Casali et al. “Achievement of highly radiating plasma in negative triangularity and effect of reactor-relevant seeded impurities on confinement and transport”. In: *Plasma Physics and Controlled Fusion* 67.2 (2025), p. 025007.
- [18] X Lin et al. “Physical mechanisms for the transition from type-III to large ELMs induced by impurity injection on EAST”. In: *Physics Letters A* 431 (2022), p. 127988.
- [19] WL Zhong et al. “Impact of impurity mixture gas seeded by supersonic molecular beam injection on edge-localized modes in the HL-2A tokamak”. In: *Nuclear Fusion* 59.7 (2019), p. 076033.
- [20] HQ Wang et al. “New edge coherent mode providing continuous transport in long-pulse H-mode plasmas”. In: *Physical review letters* 112.18 (2014), p. 185004.
- [21] GS Xu et al. “Turbulence-Driven Edge-Localized-Mode-Free High-Confinement Mode with Divertor Detachment in a Metal-Wall Tokamak”. In: *Physical Review Letters* 136.12 (2026), p. 125101.
- [22] KH Burrell et al. “Quiescent double barrier high-confinement mode plasmas in the DIII-D tokamak”. In: *Physics of Plasmas* 8.5 (2001), pp. 2153–2162.
- [23] HY Guo et al. “Recent advances in long-pulse high-confinement plasma operations in Experimental Advanced Superconducting Tokamak”. In: *Physics of plasmas* 21.5 (2014).
- [24] YL Li et al. “The simulation of ELMs mitigation by pedestal coherent mode in EAST using BOUT++”. In: *Nuclear Fusion* 62.6 (2022), p. 066018.
- [25] Zeyu Li et al. “Multi-scale interaction mechanism for edge-localized-mode suppression in the tokamak edge”. In: *Nature Communications* (2025).
- [26] Jiangang Li and Yuanxi Wan. “The experimental advanced superconducting tokamak”. In: *Engineering* 7.11 (2021), pp. 1523–1528.
- [27] YM Wang et al. “Development of the quasi-optical combiner systems for density profile reflectometers on the EAST tokamak”. In: *Fusion Engineering and Design* 148 (2019), p. 111286.
- [28] Qing Zang et al. “Upgraded multipulse laser and multipoint Thomson scattering diagnostics on EAST”. In: *Review of Scientific Instruments* 82.6 (2011).
- [29] Yong Liu et al. “Overview of the electron cyclotron emission measurements on EAST”. In: *Fusion Engineering and Design* 136 (2018), pp. 72–75.
- [30] X Feng et al. “Five-channel tunable W-band Doppler backscattering system in the experimental advanced superconducting tokamak”. In: *Review of Scientific Instruments* 90.2 (2019).
- [31] HM Xiang et al. “Development of an ordinary mode multi-channel correlation reflectometer on EAST tokamak”. In: *Review of Scientific Instruments* 89.10 (2018).
- [32] Zhen Zhou et al. “Experimental study of core and edge fluctuations by reflectometry on EAST tokamak”. In: *Plasma Science and Technology* 23.7 (2021), p. 075101.

- [33] Gongshun Li et al. “Experimental study of core MHD events in EAST advanced scenarios by microwave reflectometry”. In: *Plasma Physics and Controlled Fusion* 67.4 (2025), p. 045027.
- [34] YM Duan et al. “The resistive bolometer for radiated power measurement on EAST”. In: *Review of Scientific Instruments* 83.9 (2012).
- [35] Shanwei Hou et al. “Development of a multi-spectral extreme ultraviolet imaging diagnostics on the Experimental Advanced Superconducting Tokamak”. In: *Fusion Engineering and Design* 208 (2024), p. 114681.
- [36] Yuze Yu et al. “Identification of an edge coherent mode in an EAST electron cyclotron resonance heated H-mode plasma”. In: *Plasma Science and Technology* 27.11 (2025), p. 115103.
- [37] N Kumar et al. “ITG turbulence in gyrokinetic simulations of high collisionality spherical tokamak plasmas”. In: *Nuclear Fusion* 65.8 (2025), p. 086033.
- [38] X Jian et al. “Shafranov-shift destabilization of ballooning-type micro-instabilities”. In: *Nuclear Fusion* 65.8 (2025), p. 086038.
- [39] NT Howard et al. “Simultaneous reproduction of experimental profiles, fluxes, transport coefficients, and turbulence characteristics via nonlinear gyrokinetic profile predictions in a DIII-D ITER similar shape plasma”. In: *Physics of Plasmas* 31.3 (2024).
- [40] Zeyu Li et al. “The role of ion-scale micro-turbulence in pedestal width of the DIII-D wide-pedestal QH mode”. In: *Nuclear Fusion* 65.1 (2025), p. 016030.
- [41] NT Howard et al. “Gyrokinetic simulation of turbulence and transport in the SPARC tokamak”. In: *Physics of Plasmas* 28.7 (2021).
- [42] Xiang Jian et al. “Role of microtearing turbulence in DIII-D high bootstrap current fraction plasmas”. In: *Physical review letters* 123.22 (2019), p. 225002.